Journal of Materials Chemistry A

Accepted Manuscript

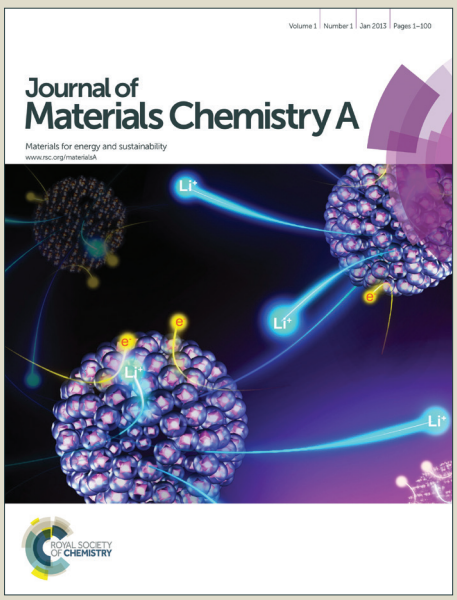

ROYAL SOCIETY OF CHEMISTRY

www.rsc.org/materialsA

Journal of Materials Chemistry A RSCPublishing

ARTICLE

3D ordered macroporous TiO_2-supported Pt@CdS core-shell nanoparticles: Design, synthesis and efficient photocatalytic conversion of CO_2 with water to methane

Cite this: DOI: 10.1039/x0xx00000x

Received 00th January 2012,
Accepted 00th January 2012

DOI: 10.1039/x0xx00000x

www.rsc.org/

Yuechang Wei,[a] Jinqing Jiao,[a] Zhen Zhao,*[a] Wenjia Zhong,[a] Jianmei Li,[a] Jian Liu,*[a] Guiyuan Jiang,[a] and Aijun Duan[a]

A series of photocatalysts of three-dimensionally ordered macroporous (3DOM) TiO_2-supported core-shell structural Pt@CdS nanoparticles were facilely synthesized by the gas bubbling-assisted membrane reduction-precipitation (GBMR/P) method. All the catalysts possess well-defined 3DOM structure with the interconnected networks of spherical voids, and the Pt@CdS core-shell nanoparticles with different molar ratios of Cd/Pt are well dispersed and supported on the inner wall of uniform macropore. 3DOM structure can enhance the light-harvesting efficiency due to increasing the distance of the light path by enhancing random light scattering. And the all-solid-state Z-scheme system with CdS(shell)-Pt(core)-TiO_2(support) nanojunction is favourable for the separation of photogenerated electrons and holes because of the vectorial electron transfer of TiO_2→Pt→CdS. 3DOM Pt@CdS/TiO_2 catalysts exhibit super photocatalytic performance for CO_2 reduction to CH_4 under the simulated solar irradiation. Among the as-prepared catalysts, 3DOM Pt@CdS/TiO_2-1 catalyst with the moderate thickness of CdS nanolayer shell shows the highest photocatalytic activity and selectivity for CO_2 reduction, e.g., its formation rate of CH_4 is 36.8 μmol g^{-1} h^{-1} and its selectivity to CH_4 production by CO_2 reduction is 98.1 %. The design and versatile synthetic approach of all-solid-state Z-scheme system on the surface of 3DOM oxides are expected to throw new light on the fabrication of highly efficient photocatalyst for CO_2 reduction to hydrocarbon.

1. Introduction

The energy crisis and the increasing atmospheric concentration of carbon dioxide (CO_2) due to overexploitation of fossil fuels are recognized to be the two major problems in the foreseeable future.[1] Solar photocatalytic conversion of CO_2 with H_2O to hydrocarbon fuels has sparked a new sustainable development path since it would help to reduce atmospheric CO_2 level and partly fulfill energy demands.[2] The chemical conversion of CO_2 to industrially beneficial compounds is advantageous in terms of Green and Sustainable Chemistry because CO_2 is an inexpensive, nontoxic and abundant C1 feedstock. However, the conversion of CO_2 with H_2O, two very stable molecules accompanied with a large positive change in the Gibbs free energy, is one of the biggest challenges in chemistry.[3] Therefore, the design and synthesis of efficient photocatalysts to enable the reduction of CO_2 for the production of fuels and chemicals has attracted much attention and is a desirable goal.[4]

The solar photocatalytic conversion of CO_2 and H_2O to produce fuels and chemicals can be realized by using active photocatalysts. Since the pioneering studies by Inoue and Fujishima, et al.[5], many studies have been devoted to the semiconductor-based photocatalytic reduction of CO_2 with H_2O and the pace has increased enormously in recent years.[6] In this heterogeneous process, the photocatalyst is usually a hybrid semiconductor material which absorbs light, separates the photogenerated charges, transports them to the surface and provides active sites for the catalytic reaction.[7] Among the various semiconductor photocatalysts, titanium dioxide (TiO_2) is the most common and promising photocatalyst for solar-fuel production by far, which is owing to its cheapness, availability, photostability and nontoxicity.[8] Photoactivity of TiO_2 derives from oxidizing holes and reducing electrons produced by exciting TiO_2 at wavelengths shorter than its ultraviolet absorption edge. Therefore, the photocatalytic activity of pure TiO_2 for the CO_2 reduction under visible light irradiation is not high enough for practical application due to the drawbacks of

the wide band gap, the low absorption efficiency of solar irradiation and the easy charge recombination.[9]

The design and development of efficient photocatalysts is a critical issue in photocatalytic CO_2 reduction, which involves light absorption, photogenerated charge transfer/separation, and the subsequent catalysis, etc. On the one hand, for improving the light harvesting, the spherical voids can increase the absorption efficiency of sunlight due to increasing the distance of the light path by enhancing random light scattering.[10] Because of a periodic dielectric contrast in the length scale of the wavelength of light, photonic crystals (PCs) materials offer a great capability of controlling and manipulating the flow of incident light. Recently, the unique optical performance of PCs for light harvesting has been attracting strong interest in photo-catalysis and photoelectrochemistry.[11] For example, three-dimensionally ordered macroporous (3DOM) TiO_2 were constructed and demonstrated super performances for photodegradation organic pollutant [12] and hydrogen evolution[13]. However, the photocatalytic efficiency of PCs with a single component for CO_2 reduction is not good enough due to the low photogenerated charge transfer/separation efficiency.

On the other hand, many strategies have been developed to improve photocatalysis efficiency, including loading of metal,[14] coupling plasmon resonance,[15] doping with ions,[16] reducing particle size and crystal facet of photocatalysts[17], etc. Among these tactics, constructing TiO_2-based heterostructure has been demonstrated effective for improving photocatalytic efficiency through promoting the photogenerated charge separation, harvesting visible light and facilitating CO_2 activation.[18] Various types of second-component semiconductor of TiO_2-based heterostructure have been reported, such as CdS,[19] CeO_2[20] and ZrO_2[21] and so on. On this basis, an electron transfer mediator (Pt,[22] Au,[23] and graphene oxide[24]) embed in the heterostructure interface can strengthen the interface charge transfer and result in a vectorial electron transfer via a Z-scheme system,[25] which can efficiently improve photogenerated charge separation and photocatalytic activity.[26] For all the above prominent advantages, the construction of three-component heterostructure combined with 3DOM structure is expected to bring excellent performance and powerful platforms for photocatalytic CO_2 reduction.

Herein, we firstly report a practical fabrication of visible light responsive all-solid-state three-component Z-scheme system with the core-shell structured Pt@CdS nanoparticles (NPs) on 3DOM TiO_2 support (3DOM Pt@CdS/TiO_2) via the gas bubbling-assisted membrane reduction-precipitation (GBMR/P) method. Our design and versatile synthetic approach can control the thickness of CdS shell over Pt core NPs at the nanoscale *via* the adjustable molar ratio of Cd/Pt. 3DOM structure can enhance the light-harvesting efficiency. And the all-solid-state Z-scheme system with CdS(shell)-Pt(core)-TiO_2(support) nanojunction is favourable for improving the separation of photogenerated electrons and holes due to the vectorial electron transfer of $TiO_2 \rightarrow Pt \rightarrow CdS$. This three-component system exhibits high photocatalytic activity for CO_2 reduction to CH_4 under the simulated solar irradiation, far exceeding those of the single- and two-component systems, as a result of vectorial electron transfer driven by the two-step excitation of TiO_2 and CdS. It suggests that 3DOM Pt@CdS/TiO_2 catalysts are an excellent system for photocatalytic reactions or surface chemical processes that occur at the interfaces of reactant and catalyst.

2. Experimental

2.1 Sample preparation

Synthesis of monodispersed PMMA microsphere, assembly of template, and preparation of 3DOM TiO_2 support by colloidal crystal template (CCT) method are similar to that described previously.[27] The typical schematic diagram is shown in Fig. S1. The dried samples were calcined to remove the CCT at an air flow of 80 ml min^{-1} in a tube furnace. The temperature-rising rate was 1 ^oC min^{-1} from room temperature to 600 ^oC which was kept for 5 h. Finally, 3DOM TiO_2 support was obtained.

3DOM Pt@CdS/TiO_2 catalysts were synthesized by two-step process of GBMR/P method. The schematic and digital photos about experimental apparatus are shown in Fig. S2 and Fig. S3, respectively. As shown in Fig. S2, the typical preparative procedures were described as follows (3DOM Pt@CdS/TiO_2 catalysts as example): The first step is the preparation of 3DOM TiO_2-supported Pt NPs via GBMR method.[28] The second step is the preparation of CdS NP coated on the surface of 3DOM Pt/TiO_2 catalyst using GBMP method.[29] The final products were calcined in an oven at 100 ^oC for 2 h and the desired 3DOM Pt@CdS/TiO_2 catalysts were obtained. The initial weight percent of Pt to TiO_2 in the catalysts were always 4 wt%. The catalysts are generically named as 3DOM Pt@CdS/TiO_2-n, where n is the theoretical molar ratio of CdS to Pt.

2.2 Physical and chemical characterization

The nitrogen adsorption/desorption isotherm measurement was carried out at −196 °C by using an automated gas sorption analyzer (Quantachrome Autosorb-iQ, USA) after having degassed the sample for 4h at 300 ℃. The specific area was calculated from the Brunauer-Emmett-Teller (BET) equation using P/P^0 values between 0.05 and 0.3. XRD patterns were measured on a powder X-ray diffractometer (Shimadzu XRD 6000) using Cu Kα (λ = 0.15406 nm) radiation with a Nickel filter operating at 40 kV and 10 mA in the 2θ range of 15-90 ^{o}. The UV-Vis DRS experiments were performed on a UV-Vis spectrophotometer (Hitachi U-4100) with the integration sphere diffuse reflectance attachment. The surface morphology of the samples was observed by SEM (FEI Quanta 200F). The TEM and HRTEM images were carried out using a JEOl JEM 2100 electron microscope equipped with a field emission source at an accelerating voltage of 200 kV. The average particle diameter was calculated from the mean diameter frequency distribution with the formula: $d=\sum n_i d_i / \sum n_i$, where n_i is the number of particles with particle diameter d_i in a certain range. The actual content of Pt in catalysts was determined by inductive coupled plasma atomic emission spectrometry (ICP-AES) (PE, OPTIMA 5300DV). X-ray photoelectron spectra (XPS) were

recorded on a Perkin-Elmer PHI-1600 ESCA spectrometer using Mg Ka (hv=1253.6 eV, 1 eV=1.603×10^{-19} J) X-ray source. The binding energies were calibrated using C1s peak of contaminant carbon (BE = 284. 38 eV) as an internal standard. Raman spectra were collected in the anti-Stokes range of 200-2000 cm^{-1} using an inVia Reflex-Renishaw spectrometer with the spectral resolution of 4 cm^{-1}. The 532 nm single-frequency He-Gd laser was used as the excitation source. The photoluminescence (PL) spectra of the as-prepared samples were measured using a Hitachi F-4600 fluorescence spectrophotometer. The solid catalysts were placed in the standard slot and were compacted by the quartz glass. The semiconductor material was firstly irradiated by the excitation light and absorbs the photon energy, and then the electron-hole pairs were produced in the semiconductor material. Finally, the recombination of electron-hole pairs on the surface of semiconductor can produce the PL emission spectra.

2.3 Activity tests

The photocatalytic reduction of CO_2 with H_2O were carried out in a gas-closed circulation system, 0.02 g of the tested catalyst was put in a glass reactor with a basal diameter of 6.5 cm by spin-coating. The light source was a 300 W Xe lamp (l=320-780 nm) using the simulated sunlight purchased from Perfect Light Co. Light was passed through a quartz window and circulated cooling water was applied to absorb the infrared portion of the Xe lamp irradiation. The intensity of incident light at the location of catalyst was measured to be 100 mW cm^{-2} by a spectroradiometer. The light is perpendicular to the surface of spectroradiometer, and the distance between light source and spectroradiometer is 30 cm, which is same as the process of activity tests. The volume of the reaction system was about 500 mL. The reaction setup was vacuum-treated several times, and then the high purity of CO_2 gas was flowed into the reaction setup for reaching ambient pressure. Compressed CO_2 (99.999%) regulated by a rotor flowmeter (at a flow rate of 15 mL min^{-1}) was passed through a deionized water bubbler to introduce CO_2 and water vapor mixture into the photoreactor that has a quartz window at constant temperature (20 ^{o}C). The pressure of CO_2 was regulated to 0.1 MPa. Before irradiation, the as-prepared photocatalysts were kept in the CO_2-H_2O atmosphere for several hours to ensure the absorption of gas molecules for equilibrium. The photocatalytic reduction of CO_2 with H_2O was typically carried out at 298 K for 2 h in each run. The products were analyzed by using an on-line gas chromatograph (GC-9560; HuaAiSePu Corp., China) equipped with two automated gas sampling valves, a thermal conductivity detector (TCD) with 5A column for product analysis of H_2 and O_2 and a flame ionization detector (FID) with TDX-01 column for product analysis of CO and CH_4. The quantification of the products was based on the external standard with the use of a calibration curve. The catalytic activity was evaluated by the formation rate of H_2, CO and CH_4, selectivity for CO_2 reduction with H_2O.

The harvesting efficiency (apparent quantum efficiency, QE) was measured under the same photocatalytic reaction condition, with particular irradiation light at 420 nm using a Xe lamp with 420 nm band-passfilter (full width at half maximum 15 nm) and UV cutoff filter as light sources, and the incident flux was determined by Radiometer (FZ-A, Photoelectric Instrument Factory of Beijing Normal University). The harvesting efficiency was calculated according to the following Eq.:

$$QE[\%] = \frac{\text{number of reacted electrons}}{\text{number of incident photons}} = \frac{\text{number of } H_2 \times 2 + \text{number of } CH_4 \times 8 + \text{number of CO} \times 2}{\text{number of incident photons}} \times 100\%$$

3. Results and discussion

3.1 The characterization results of catalysts

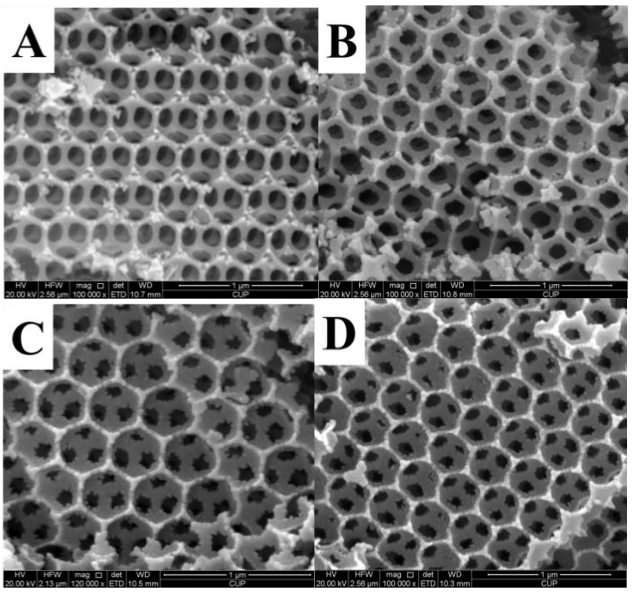

Fig. 1 SEM images of 3DOM TiO_2 and Pt@CdS/TiO_2 catalysts prepared by GBMR/P method. A. TiO_2; B. Pt@CdS/TiO_2-1; C. Pt@CdS/TiO_2-2; D. Pt@CdS/TiO_2-4

Fig. 1 shows SEM images of 3DOM TiO_2 and Pt@CdS/TiO_2 catalysts with different Cd/Pt molar ratios obtained by two step processes of the GBMR/P method. The images exhibit that the materials are macroporous structure, containing periodic voids with average diameter of 310±10 nm and wall thickness of 30±5 nm, which corresponds to shrinkage of 20-30% compared with the initial size (420 nm) of PMMA microspheres (Fig. S4). The macroporous structure of 3DOM Pt@CdS/TiO_2 materials is similar to that of 3DOM TiO_2 support. It indicates that the synthesis process of GBMR/P method with gas bubbling-assisted stirring operation less destroys 3DOM structure. The next layer is highly visible in SEM image and the voids are interconnected through open window, ca. 140±5 nm in diameter (Fig. 1A). However, with increasing of Cd/Pt molar ratio, the size of open window decreases. It indicates that the CdS nanolayer desposited on the surface of 3DOM Pt/TiO_2 support, and too much CdS nanolayer can affect the macroporous structure. In addition, the BET surface areas of 3DOM TiO_2, Pt/TiO_2 and Pt@CdS/TiO_2 catalysts are summarized in Table 1.

The BET surface area of 3DOM TiO_2 support is 49 m^2 g^{-1}. With the increasing of Cd/Pt ratio, the BET surface area slightly decreases. 3DOM Pt@CdS/TiO_2 catalysts will be hereafter considered as one of the suitable systems with the high catalytic activity for CO_2 reduction with H_2O.

Table 1 The crystal parameters and average crystal sizes of 3DOM TiO_2, Pt/TiO_2 and Pt@CdS/TiO_2 catalysts.

Catalyst	D [a] of TiO_2 (nm)	Pt size [b] (nm)	S_{BET} [c] (m^2 g^{-1})	Pt content [d] (wt%)	Eg(eV)
TiO_2	19.0	-	49	-	2.85
Pt/TiO_2	19.9	3.8	49	3.4	2.06
Pt@CdS/TiO_2-1	19.6	3.9	46	3.3	1.98
Pt@CdS/TiO_2-2	19.2	4.0	47	3.1	1.93
Pt@CdS/TiO_2-4	19.6	4.0	46	3.0	1.86

[a] Determined by XRD using Scherrer equation with the intensity of the most prominent peak, (101). [b] Determined by HRTEM. [c] Surface area obtained by BET method; [d] Determined by ICP-AES.

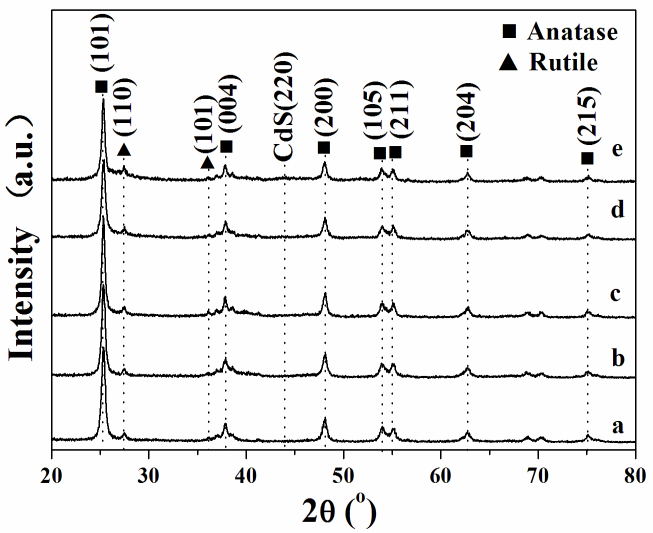

Fig. 2 XRD patterns of 3DOM TiO_2, Pt/TiO_2 and Pt@CdS/TiO_2 catalysts prepared by GBMR/P method. a. TiO_2; b. Pt/TiO_2; c. Pt@CdS/TiO_2-1; d. Pt@CdS/TiO_2-2; e. Pt@CdS/TiO_2-4

Fig. 2 shows the XRD patterns of 3DOM TiO_2, Pt/TiO_2 and Pt@CdS/TiO_2 catalysts. The diffraction peaks (2θ) at 25.3, 37.8, 48.0, 53.9, 55.1, 62.7 and 75.0 ° can be indexed to the (101), (004), (200), (105), (211), (204) and (215) crystal faces of 3DOM TiO_2 with a tetragonal anatase structure (PDF# 21-1272), respectively. And the weak diffraction peaks (2θ) at 27.4 and 36.1 ° can be indexed to the (110) and (101) crystal faces of 3DOM TiO_2 with a tetragonal rutile structure (PDF# 65-0191). It indicates the coexistence of the two crystal phases' structures for 3DOM TiO_2 support, which is similar to the phase structure of P25 (Fig. S5). After loading Pt@CdS core-shell NPs, the extremely weak diffraction peaks (2θ) at 44.0 ° over 3DOM Pt@CdS/TiO_2-4 catalysts can be observed, which is indexed to the (220) crystal faces of CdS with a cubic hawleyite structure (PDF # 10-0454), and the characteristic diffraction peaks belonging to supported Pt NPs were not detected. It indicates that the sizes of supported Pt and CdS NPs on the surface of 3DOM TiO_2 may be beyond the detection limit of XRD spectra (<4 nm). The average crystalline size of 3DOM TiO_2 determined by Scherrer equation is about 19.0 nm. No obvious change of its crystalline size is observed after Pt and CdS NPs supported on 3DOM TiO_2.

Fig. 3 shows the TEM and HRTEM images of 3DOM Pt/TiO_2 and Pt@CdS/TiO_2 catalysts. 3DOM structure with overlapped pores can be clearly observed by TEM images after the loading Pt and Pt@CdS NPs. The walls of the macroporous samples are crystalline according to the selected area electron diffraction (SAED) (inset in Fig. 3A). The characteristic SAED rings of TiO_2 oxide from inside to outside are indexed as (101), (004) and (200) planes of a tetragonal structure, respectively. It is in accord with the result of XRD characterization. A mass of bare Pt NPs deposited on the surface of 3DOM TiO_2 can be clearly observed in TEM and HRTEM image of Fig. 3B, and the Pt NPs are highly dispersed and uniform in size. The Pt NP size is in the range of 2~6 nm with a narrow distribution and a mean diameter of 3.8 nm by statistical analyses of 100 Pt NPs (Fig. S6). As shown in inset of Fig. 3B, the clear lattice fringes of one Pt particle were clearly observed, and the Fast Fourier Transform (FFT) image indicates that the spherical Pt particles located on the surface of TiO_2 are crystalline and exposed (111) crystal faces of face-centered-cubic (fcc) structure. The results indicate that there is a tight contact between TiO_2 support and Pt NPs, which provides a good basis for efficient electron transfer and subsequent coating of CdS nanolayers.

After coating CdS on Pt NPs, 3DOM structure keeps well (Fig. 3C, 3E and 3G), and supported Pt-CdS NPs are still highly dispersed and uniform in size. As shown in Fig. 3D, it clearly shows a core-shell structure with two different lattice fringes on the core and shell, and the marked lattice fringes of 3.3 Å on the shell and 2.3 Å on the core are indexed as (111) planes of CdS nanolayer and Pt NP, respectively, indicating the formation of the core-shell structural Pt@CdS NPs. And the thickness of the CdS nanoshell over Pt NPs is in the range of 1-2 nanometres. With the increasing of Cd/Pt molar ratio, the thickness of the CdS nanoshell deposited on the surface of Pt NPs increases remarkably (Fig. 3F and 3H). The ordered nanostructure with Pt@CdS core-shell-type NPs would provide abundant catalytic activity sites due to the maximal contact region of CdS(shell)-Pt(core)-TiO_2(support) nanojunction system at the atomic level. The sizes of Pt@CdS core-shell NPs over 3DOM TiO_2 are in the range of 3-9 nm with a narrow distribution, and the mean diameters of Pt core are 3.9±0.1 nm by statistical analyses of the Pt@CdS core-shell NPs and the results are shown in Table 1. It indicates that the size of supported Pt NPs and the thickness of CdS nanolayers could be effectively controlled by the GBMR/P method. These results demonstrate that the CdS shell is coated selectively on the surface of Pt NPs and a CdS-Pt-TiO_2 heterostructure system

was constructed successfully. The selective deposition and high-quality coating ensure the efficient photogenerated electron transfer and the subsequent photocatalysis.

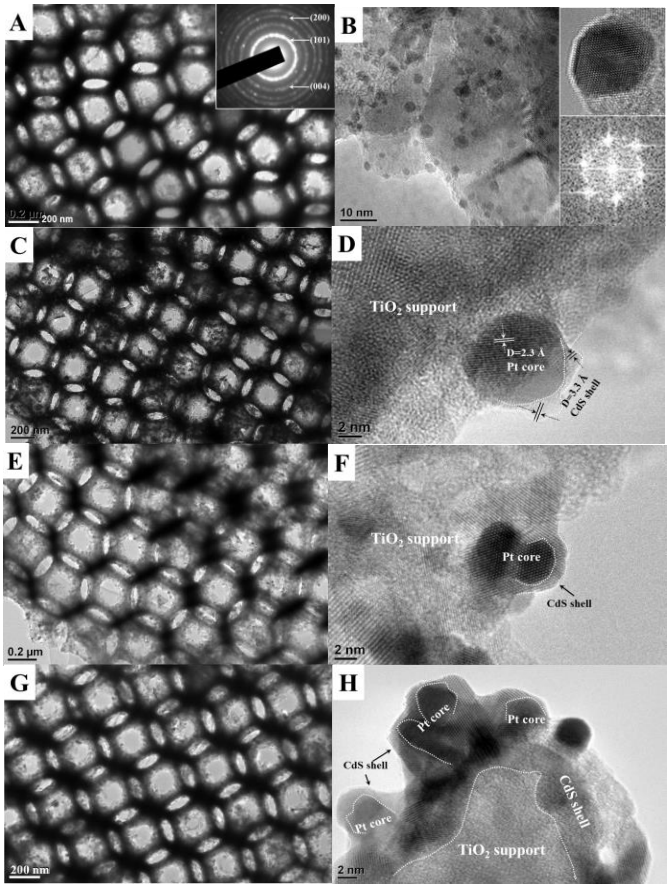

Fig. 3 TEM and HRTEM images of 3DOM Pt/TiO_2 (A-B), $Pt@CdS/TiO_2$-1 (C-D), $Pt@CdS/TiO_2$-2 (E-F) and $Pt@CdS/TiO_2$-4 (G-H) catalysts. The inset in TEM image of (A) is the corresponding SAED pattern.

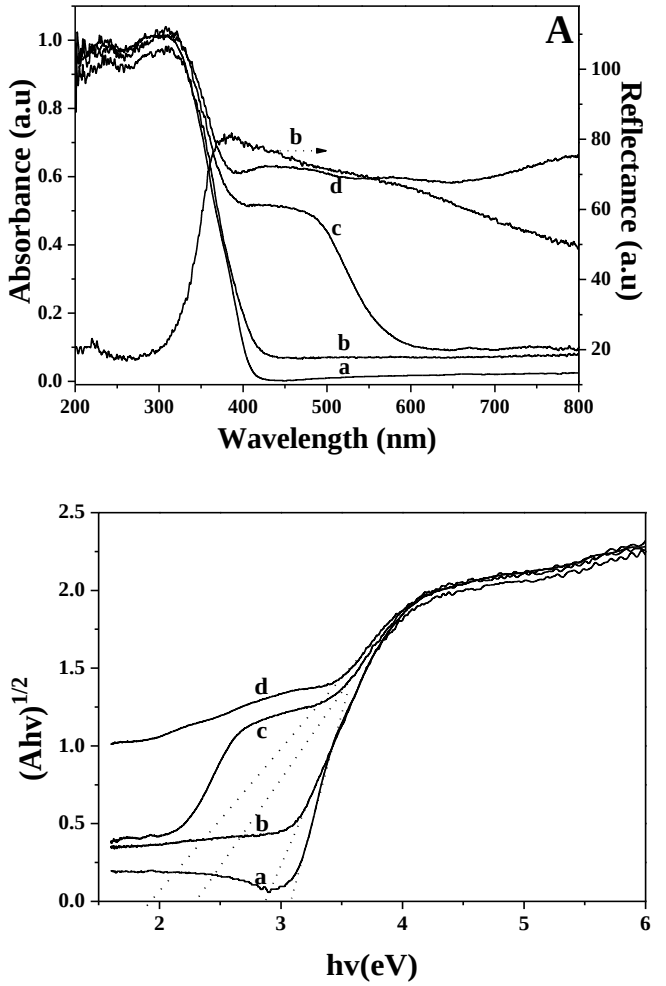

Fig. 4 UV-Vis DRS (A) and Kubelka-Munk transformed reflectance spectra to estimate optical absorption band gap (B) of commercial-P25(a), 3DOM TiO_2(b), CdS/TiO_2(c) and $Pt@CdS/TiO_2$-1(d) catalysts. Fig. 4A shows simultaneously the absorbance spectra of crushed TiO_2 (Left) and the reflectance spectrum of the 3DOM photonic crystal film with stop bands maxima at 390 nm (Right).

3DOM structure can block light in a certain wavelength range, allowing the confinement and manipulation of photons in the materials. In order to investigate the periodic effect of 3DOM catalysts on the light harvesting, UV-Vis diffuse reflectance spectroscopy (DRS) studies were performed on 3DOM TiO_2, Pt/TiO_2 and $Pt@CdS/TiO_2$ catalysts and the results are shown in Fig. 4 and Fig. S8. For comparison, a commercial TiO_2 powers (P25) was also included. Interestingly, 3DOM TiO_2 displays a slight red shift of light absorption compared with the commercial P25 which absorbs light with wavelength shorter than 400 nm, and 3DOM TiO_2 has strong stop band maxima at 390 nm which is near the electronic absorption edge. The phenomenon may be ascribed to 3DOM structure, enlarged surface area and multiple scatting enable it to harvest light much more efficiently. And the strong Bragg reflection peaks indicate that it formed high-quality inverse opal structure in a wide range. After supporting Pt, CdS and Pt@CdS NPs, the catalysts show spectral response in a broad visible region (400~800 nm) owing to the photosensitizing effect of Pt and CdS. It is worthy to note that 3DOM $Pt@CdS/TiO_2$ catalysts exhibit a much stronger absorption in both ultraviolet and visble-light regions than that of 3DOM TiO_2, and this enhanced light-trapping effect is attributed to the CdS and Pt NPs. With increasing the molar ratio of CdS to Pt, the absorption region (400~600 nm) extends remarkably, indicating that the catalysts show the good response ability for visible light. The band gap of above samples could be calculated by using the equation: $(\alpha hv)^n=A(hv-Eg)$, where α is the absorption coefficient, A is the parameter that related to the effective masses associated with the valence and conduction bands, n is 1/2 for a direct transition, hv is the absorption energy, and Eg is the band gap energy.[30] Plotting $(\alpha hv)^{1/2}$ versus hv based on the spectral response in Fig. 4A gives the extrapolated intercept corresponding to the Eg value, and the results are shown in Fig. 4B. As shown in Fig. 4B, the Eg value (2.85 eV) of 3DOM TiO_2 catalyst is much smaller than that of commercial P25 (3.10 eV), which is consistent with the DRS result. And the Eg value of 3DOM CdS/TiO_2 catalyst (trace c)

is 2.30 eV. It indicates that the addition of CdS resulted in the appearance of an additional absorption band in the visible region, the intensity monotonically increased with an increase of CdS content. Moreover, the optical band gap energies of 3DOM Pt@CdS/TiO_2-1, Pt@CdS/TiO_2-2, and Pt@CdS/TiO_2-4 catalysts (1.98, 1.93, and 1.86 eV, respectively) display obviously red-shift compared with those of Pt/TiO_2 (2.06 eV) and CdS/TiO_2 (2.30 eV). It is very interesting to observe that the shapes of the absorption spectra for 3DOM Pt@CdS/TiO_2 catalysts are combinations of the absorption spectra of the three components. Therefore, the results indicate that the enhanced ability to absorb visible-light of 3DOM Pt@CdS/TiO_2 catalysts makes them as a promising photocatalyst for solar-driven applications.

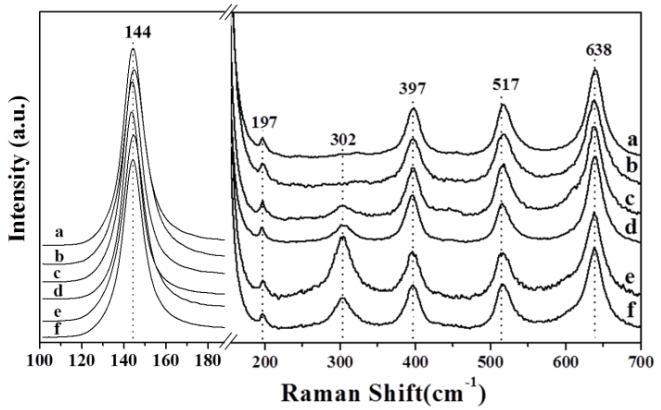

Fig. 5 Raman spectra of 3DOM TiO_2, Pt/TiO_2, Pt@CdS/TiO_2 and CdS/TiO_2 catalysts with the 532 nm laser. a. TiO_2; b. Pt/TiO_2; c. Pt@CdS/TiO_2-1; d. Pt@CdS/TiO_2-2; e. Pt@CdS/TiO_2-4; f. CdS/TiO_2

It is well-known that Raman spectroscopy is extremely sensitive to crystalline forms of TiO_2 and CdS owing to its strong scattering properties. The phase structure of 3DOM TiO_2, Pt/TiO_2, Pt@CdS/TiO_2 and CdS/TiO_2 catalysts can be further identified by Raman spectra with the 532 nm laser as the excitation source and the results are presented in Fig. 5. It can be seen that the pure TiO_2 shows major Raman bands at 144, 397, 517, and 638 cm^{-1}, which can be attributed to the Raman-active modes of anatase phase with the symmetries of Eg, B1g, A1g, and Eg, respectively.[31] And the weak Raman bands at 197 cm^{-1} can be attributed to the Raman-active modes of rutile phase. It indicates the coexistence of the two crystal phases' structures for 3DOM TiO_2, which is similar to the results of XRD. For 3DOM Pt/TiO_2 catalyst, no new Raman bands are observed in comparison with 3DOM TiO_2 catalyst. After deposition of CdS nanolayers on the surface of 3DOM Pt/TiO_2, one characteristic peaks of CdS at 302 cm^{-1} appeared, which corresponds to the first-order longitudinal optical (1LO) phonon modes of hexagonal CdS.[32] The peak at ~243 cm^{-1}, which assigns to cubic CdS, was not observed, suggesting that the CdS in Pt@CdS/TiO_2 composites only exists in hexagonal structure. The formation of hexagonal CdS nanolayers might be ascribed to the influence of the TiO_2 substrate, although the cubic phase is more stable at room temperature.[33] And with the increasing of CdS loading amount, the relative peak intensity of CdS to TiO_2 increases. It indicates that the deposited CdS amount on the surface of the Pt/TiO_2 increases, and a shell of CdS nanolayer forms, which is conducive to improving the photocatalytic performance due to the CdS(shell)-Pt(core)-TiO_2(support) nanojunction with the efficient separation of photogenerated electrons and holes.[23] It is in agreement with the result of TEM images. The CdS-Pt-TiO_2 heterojunction with the suitable thickness can improve the photocatalytic performance for the reduction of CO_2 with H_2O.

To examine the effect of CdS(shell)-Pt(core)-TiO_2(support) nanojunction structure on the electronic properties of the surface elemental (Pt, Cd and S), 3DOM Pt/TiO_2, Pt@CdS/TiO_2 and CdS/TiO_2 catalysts were studied by XPS, and the results are shown in Fig. 6. And the Ti 2p and O 1s XPS spectra of all catalysts are shown in Fig. S9. As shown in Fig. 6A, with increasing of CdS shell thickness, the intensities of Pt 4f XPS peaks decrease, while the peak intensities of S 2P and Cd 3d increase (Figs. 6B and 6C). It indirectly indicates that the CdS layers deposited on the surface of Pt NPs and the formation of Pt@CdS core-shell NPs. For clear comparison, the intensity of c and d curves are magnified to 1.5 and 2.0 times in Fig. 6A, respectively. The deconvolutions of the spectra were made by the standard procedure, the binding energies of 70.2 and 73.5 eV, 71.2 and 74.8 eV, 74.1 and 76.9 eV have been assigned to Pt^0, Pt^{2+} and Pt^{4+} species, respectively, indicating that both metallic (Pt^0) and ionic platinum ($Pt^{\delta+}$) species are present on the surface of 3DOM TiO_2. The appearances of ionic $Pt^{\delta+}$(Pt^{2+} and Pt^{4+}) species are attributed to the electron transfer from Pt^0 to S^{2-} or O^{2-} for the strong metal (Pt)-support (CdS and TiO_2) interaction (SMSI),[34] and the interface areas of Pt@CdS core-shell NPs are far larger than that of supported bare Pt catalyst. Meantime, the SMSI can decrease the total energy of TiO_2-Pt-CdS three-component nanojunction system, which is conducive to improving the vectorial electron transfer driven by the two-step excitation of TiO_2 and CdS.[23] And the relative amount of each Pt species (Pt^0, Pt^{2+} and Pt^{4+}) on the surface of catalysts were estimated by the Pt 4f XPS, and the results are presented in Table 2. The $Pt^{\delta+}$ concentration of 3DOM Pt@CdS/TiO_2 catalysts are beyond 44 % at the atomic ratio, but that of 3DOM Pt/TiO_2 catalyst is only 26 %. It can be noticed that 3DOM Pt@CdS/TiO_2-1 catalyst shows the largest ratio of $Pt^{\delta+}$ species, indicating that the thickness of CdS nanolayers can effectively enhance the SMSI between Pt core and CdS shell. As shown in Fig. 6B, high-resolution XPS of S 2p with binding energy of 160.8 eV (S 2p 3/2) and 161.8 eV (S 2p 1/2) are ascribed to the hybrid chemical bond species of S^{2-} and Cd-S^- arising from Pt@CdS core-shell NPs. And high-resolution XPS spectra of Cd 3d with featured peaks of 411.2 eV (Cd 3d 3/2) and 404.4 eV (Cd 3d 5/2) (Fig. 6C) reveal that the Cd element is oxidation state (Cd^{2+}).[35] It indicates that the CdS shell layers were successfully synthesized and deposited on the surface of 3DOM Pt@CdS/TiO_2 catalysts.

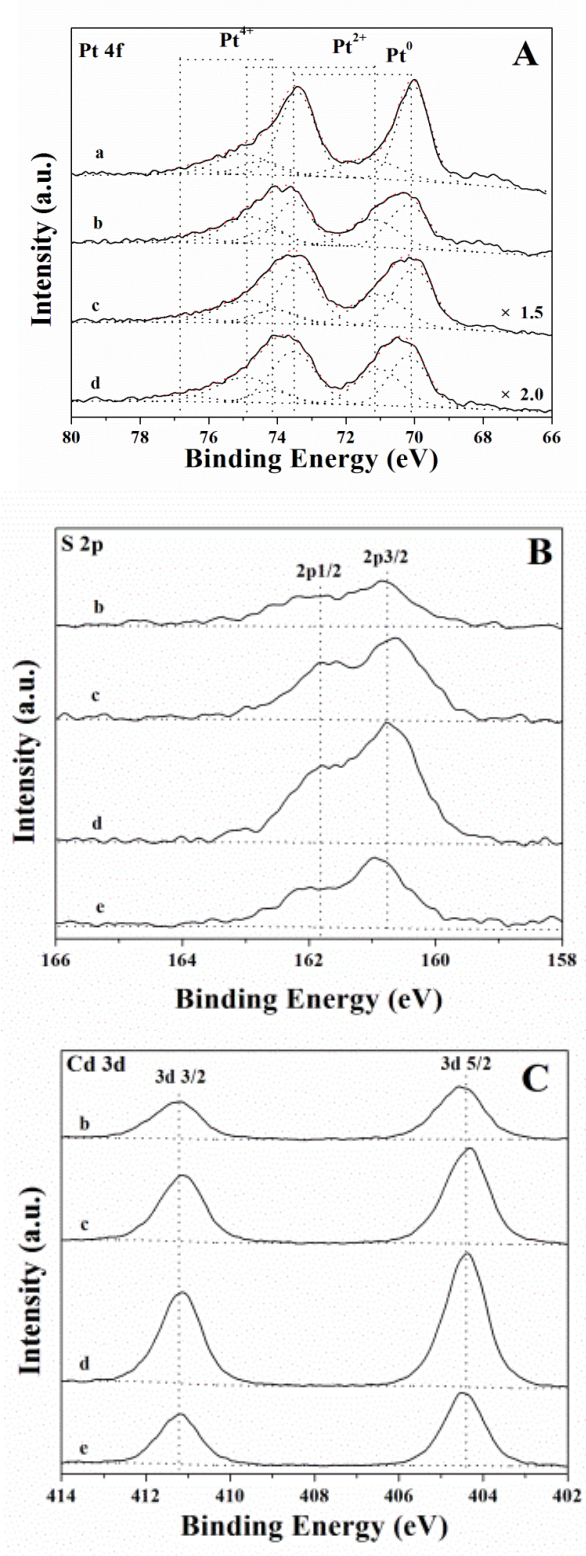

Fig. 6 X-ray photoelectron spectra (XPS) of Pt 4f (A), S 2p (B) and Cd 3d (C) regions for 3DOM Pt_4/TiO_2, $Pt@CdS/TiO_2$ and CdS/TiO_2 catalysts. For clear comparison, the intensity of c and d curves in Pt 4f (A) figure are magnified to 1.5 and 2.0 times, respectively. a. Pt_4/TiO_2; b. $Pt@CdS/TiO_2$-1; c. $Pt@CdS/TiO_2$-2; d. $Pt@CdS/TiO_2$-4; e. CdS/TiO_2

Table 2 Surface compositions and oxidation states of O, Pt and Ce species derived from XPS analyses.

Sample (3DOM)	Pt species (%)			
	Pt^0	Pt^{2+}	Pt^{4+}	$Pt^{\&+\,a}$
Pt/TiO_2	73.5	19.4	7.1	26.5
$Pt@CdS/TiO_2$-1	48.2	39.0	12.8	51.8
$Pt@CdS/TiO_2$-2	51.5	38.1	10.4	48.5
$Pt@CdS/TiO_2$-4	54.4	34.6	10.0	44.6

[a] The $Pt^{\&+}$ values are equal to the sum of Pt^{2+} and Pt^{4+}.

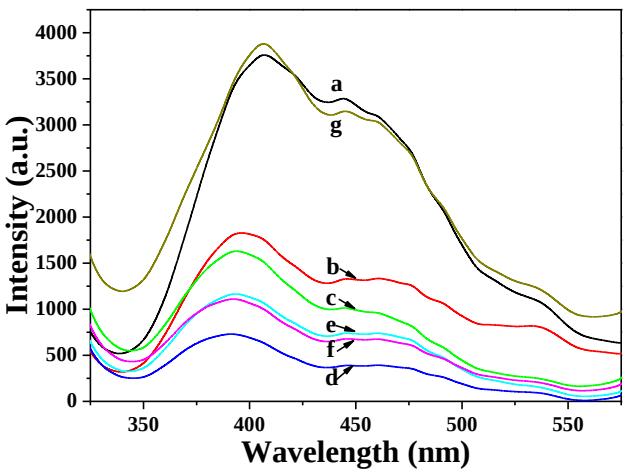

Fig. 7 Photoluminescence (PL) spectra of 3DOM TiO_2, CdS/TiO_2, Pt/TiO_2 and $Pt@CdS/TiO_2$ catalysts, λ_{Ex}=300 nm. a. TiO_2; b. CdS/TiO_2; c. Pt/TiO_2; d. $Pt@CdS/TiO_2$-1; e. $Pt@CdS/TiO_2$-2; f. $Pt@CdS/TiO_2$-4; g. P25

Photoluminescence (PL) spectra are usually used to explore the efficiency of the charge carrier trapping, migration, and transfer, and it is quite helpful to understand the fate of electron-hole pairs in semiconductor particles as PL emission arises from the recombination of free carriers.[36] The intensity of the PL emission spectra depends on the recombination of excited electrons and holes. The lower the PL emission intensity is, the lower the recombination property of the samples is. Fig. 7 shows the PL spectra of 3DOM TiO_2, CdS/TiO_2, Pt/TiO_2 and $Pt@CdS/TiO_2$ catalysts. The excitation wavelength was set at 300 nm. For comparison, the PL spectrum of P25 is also included. The PL emission intensity of P25 is higher than that of 3DOM TiO_2 catalyst, indicating that 3DOM TiO_2 catalyst has the lower recombination rate of photoinduced electron-hole pairs. It can be observed that 3DOM TiO_2 catalyst shows the strong emission peaks during 390~430 nm and 440~500nm at ambient temperature, which might be attributed to the emission of the bandgap transition of 2.85 eV and that of the charge transfer transition of oxygen vacancy trapped electrons, respectively.[37] After introduction of Pt NPs and CdS nanolayers, their PL emission intensities obviously decrease, indicating that the tri-coupling of TiO_2, Pt

and CdS in the heterostructures effectively diminished the recombination of photogenerated electron-hole pairs, which is beneficial to improving the photocatalytic activity for CO_2 reduction. Among the studied catalysts, 3DOM Pt@CdS/TiO_2-1 catalyst shows the lowest recombination efficiency of photoinduced electron-hole pairs, indicating that the suitable ratio of Pt and CdS can optimize the recombination efficiency of photogenerated electron-hole pairs.

3.2 Photocatalytic activity for CO_2 reduction under simulated solar irradiation

The measurements for photocatalytic reduction of CO_2 with H_2O were carried out in a gas-closed circulation system with a continuous-flow mode under simulated light irradiation. CO_2 and water vapor sealed in the system, and samples were continually taken from the reaction cell at given intervals (40 min) for quantitative analysis based on the external standard by using calibration curve. Commercial P25 was selected as the reference catalyst in photoreduction of CO_2. With a mixture of CO_2 and H_2O vapor passing through the reactor, the background test was first performed. No CO_2 conversion products were detected under light in the absence of photocatalysts. Moreover, without light no hydrocarbon was detected even if there is a great amount of efficient catalysts. The background tests were also performed using a mixture of pure N_2 and H_2O vapor as the feed gas with 3DOM TiO_2 and Pt@CdS/TiO_2 catalysts in the reactor under simulated light irradiation, and again, no formation of carbon-containing products were observed. In addition, the analyses of ^{13}C isotopic tracing via GC-MS for the products of photocatalytic $^{13}CO_2$ reduction over 3DOM Pt@CdS/TiO_2 catalyst after 20 h irradiation were carried out and the results are shown in Fig. S10. It shows that the peak with m/z of 17 could be recognized as $^{13}CH_4$, and the peak with m/z of 29 could be attributed to ^{13}CO. It indicates that the C element in the product of CO and CH_4 comes from CO_2 reactant. Therefore, we assert that the conversion products were derived from CO_2 in the feed gas rather than the photo-decomposition of residue organics in the catalysts. According to the tests, we can learn that the process of CO_2 reduction requires both photocatalysts and simulated light irradiation.

The photocatalytic reduction of CO_2 with H_2O over the studied catalysts provided CO and CH_4 as two main carbon products, and the formation of H_2 and O_2 was also observed at the same time. As shown in Table 3, 3DOM TiO_2 catalyst shows higher catalytic activity than that of commercial P25, and the apparent quantum efficiency (QE) value of 3DOM TiO_2 (1.8 %) is higher than that of P25 (1.3 %), indicating that 3DOM Ti-based catalyst is a high efficiency photocatalytic system for CO_2 reduction and 3DOM structure can obviously improve the light harvesting efficiency. For 3DOM CdS/TiO_2 and Pt/TiO_2 catalysts, the loading of CdS or Pt single co-catalysts onto 3DOM TiO_2 can promote the formation of CO and CH_4 (H_2), respectively. 3DOM CdS/TiO_2 catalyst shows the higher CO production rate (4.7 μmol g^{-1} h^{-1}), which arises from the enhanced charge-separation efficiency due to the electron transfer from CdS to TiO_2.[38] And 3DOM Pt/TiO_2 catalyst presents the highest formation rate of H_2 (61.8 μmol g^{-1} h^{-1}) during 120 min light irradiation. It is attributed to the enhanced electron-hole separation through trapping electrons by the noble metal co-catalyst with a lower Fermi energy level. The increased electron density on the co-catalyst may be in favor of the formation of H_2 and CH_4 which requires eight electrons. Considering that the reduction of H_2O to H_2 is a competitive reaction with the reduction of CO_2 to CO and CH_4,[22] we have evaluated the selectivity for CO_2 reduction on an electron basis. It becomes clear that the Pt co-catalyst decreases the selectivity, whereas the selectivity for CO_2 reduction increases from 60.8 to 71.0 % by loading CdS onto TiO_2. Although CdS is a selective cocatalyst for the reduction of CO_2, the rate of CH_4 formation over CdS/TiO_2 is lower than that over 3DOM Pt/TiO_2 catalyst.

Table 3 The formation rate of H_2, CO and CH_4, the selectivity for CO_2 reduction, CO and CH_4 productions, and the apparent quantum efficiency (QE) for photocatalytic conversion of CO_2 with H_2O over 3DOM Pt/TiO_2, Pt@CdS/TiO_2 and CdS/TiO_2 catalysts.[a]

Sample (3DOM)	Formation rate [μmol g^{-1} h^{-1}]				Selectivity for CO_2 reduction (%)[b]	S_{CO} (%)[c]	S_{CH4} (%)[c]	QE (%)[e]
	H_2	O_2	CO	CH_4				
P25	3.8	N.d.[d]	1.8	1.3	64.8	58.1	41.9	1.3
TiO_2	5.6	N.d.	2.7	1.5	60.8	64.3	35.7	1.8
CdS/TiO_2	4.2	N.d.	4.7	1.4	71.0	77.0	23.0	2.0
Pt/TiO_2	61.8	55.8	0.1	4.8	23.8	2.0	98.0	10.1
Pt@CdS/TiO_2-0.5	25.7	65.3	0.3	15.6	70.9	1.8	98.2	16.3
Pt@CdS/TiO_2-1	16.2	98.7	0.7	36.8	90.1	1.9	98.1	22.6
Pt@CdS/TiO_2-2	15.6	86.5	0.9	28.4	88.0	3.1	96.9	15.5
Pt@CdS/TiO_2-4	13.5	56.6	3.0	18.6	85.1	13.9	86.1	11.6

[a] Reaction conditions: photocatalyst, 0.02 g; CO_2 pressure, 0.1 MPa; H_2O, 1.0 mL; light source, 320~780 nm; irradiation time, 2h; reaction temperature, 20 °C. [b] The selectivity was evaluated on an electron basis, equation: Selectivity (%) = $[2n(CO) + 8n(CH_4)]/[2n(CO)+8n(CH_4)+ 2n(H_2)] \times 100\%$. [c] Based on the ratio of [CO] or [CH_4] amounts to sum ([CO]+[CH_4]) amounts. [d] Not determined. [e] The apparent quantum efficiency.

3DOM Pt@CdS/TiO_2 catalysts containing core-shell-structured Pt@CdS NPs exhibit high activity for the formation of CH_4 (Table 3). Among the as-prepared catalysts, 3DOM Pt@CdS/TiO_2-1 catalyst shows the highest formation rate of CH_4 (36.8 μmol g^{-1} h^{-1}) and the low formation rate of CO (0.7 μmol g^{-1} h^{-1}), its selectivity to CH_4 production by CO_2 reduction is 98.1 %. And the apparent quantum efficiency (QE) of 3DOM Pt@CdS/TiO_2-1 catalyst was 22.6 % which was the largest value of light harvesting efficiency. The formation rate of CH_4 over 3DOM Pt@CdS/TiO_2-1 catalyst is about 24 times higher than that of 3DOM TiO_2 alone, and is 26 and 7 times in comparison with those of 3DOM CdS/TiO_2 and Pt/TiO_2

catalysts, respectively. With increasing of CdS loading, the formation rate of CH_4 decreases and the formation rate of CO increases, indicating that the thickness of CdS shell on the Pt core has a significant impact on the catalytic activity and selectivity for CO_2 reduction. The formation rate of CO over 3DOM Pt@CdS/TiO_2 catalyst was also higher than that over Pt/TiO_2. We performed a blank reaction using a mixture of pure N_2 and H_2O vapor as the feed gas with 3DOM Pt@CdS/TiO_2-1 catalysts in the reactor under simulated light irradiation. The formation of CO and CH_4 was not detected, indicating that CO and CH_4 come from CO_2 reduction. The formation rate of H_2 in the absence of CO_2 is 22.0 μmol g^{-1} h^{-1}, which is slightly higher than the result (16.2 μmol g^{-1} h^{-1}) in the presence of CO_2. It clearly demonstrates that the Pt@CdS core-shell structure suppressed the reduction of H_2O to H_2 and preferentially accelerated the reduction of CO_2 to CO and CH_4. Moreover, we further confirmed the formation rate of O_2 over the as-prepared catalysts. Among all the catalysts, 3DOM Pt@CdS/TiO_2-1 catalyst shows the highest formation rate of O_2 (98.7 μmol g^{-1} h^{-1}), which is higher than the stoichiometric rate according to the calculation of other production (81.6 μmol g^{-1} h^{-1}).[22] It may be attributed to the formation of other undetected hydrocarbon. The selectivity for CO_2 reduction over 3DOM Pt@CdS/TiO_2 catalysts is greater than 85 %. Therefore, it is concluded that the moderate thickness of CdS shell on the surface of Pt core is favorable for the reduction of CO_2 and can enhance the formation rate of CH_4.

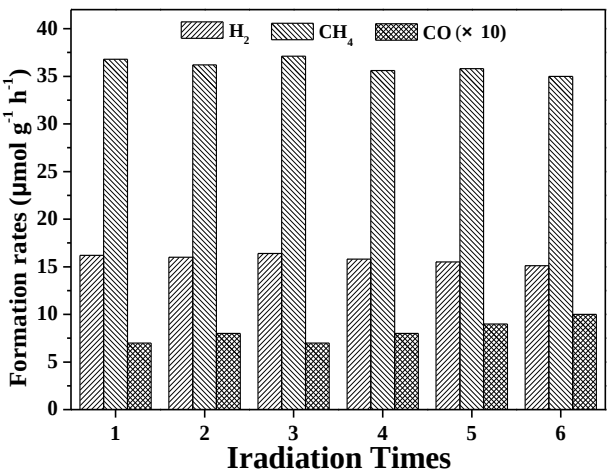

Fig. 8 Stability study on the formation rate of H_2, CH_4 and CO over 3DOM Pt@CdS/TiO_2-1 catalyst for six test cycles. In order to clearly show the CO formation rate, the values are magnified to 10 times. Reaction conditions: photocatalyst, 0.02 g; CO_2 pressure, 0.1 MPa; H_2O, 1.0 mL; light source, 320~780 nm; irradiation time, 2h; reaction temperature, 20 °C.

We further investigated the stability of photocatalytic activity for the formation rate of H_2, CH_4 and CO over 3DOM Pt@CdS/TiO_2-1 catalyst via six test cycles, and the results are shown in Fig. 8. 3DOM Pt@CdS/TiO_2-1 catalyst maintains its high catalytic activities for the photocatalytic reduction of CO_2 with H_2O in six test cycles, i.e., the formation rate of H_2, CH_4 and CO in the sixth test cycle are 15.1, 35.2 and 1.0 μmol g^{-1} h^{-1}, respectively, which has not obviously changed in comparison with the first cycle values (Table 3). Based on the results of SEM (Fig. S11), and TEM (Fig. S12), it is proved that, after the six test cycles of photocatalytic reduction of CO_2 with H_2O, the structure of macropore and Pt@CdS core-shell nanoparticles over 3DOM Pt@CdS/TiO_2-1 catalyst have not obviously changed in comparison with the fresh catalyst. Fig. S13 shows the S2p XPS of fresh 3DOM Pt@CdS/TiO_2-1 catalyst and used one after the six test cycles for photocatalytic reduction of CO_2 with H_2O. The positions of their binding energies located at 160.8 eV (S 2p 3/2) and 161.8 eV (S 2p 1/2) have not changed, indicating that the electronic property of S element is S^{2-}. Therefore, it is proved that 3DOM Pt@CdS/TiO_2 catalysts have the good stability of structure and photocatalytic activity for the CO_2 reduction with H_2O under the simulated solar irradiation.

3.3 Discussion on the photocatalytic mechanism of 3DOM Pt@CdS/TiO_2 catalysts for CO_2 reduction with H_2O

During photocatalytic CO_2 reduction with H_2O vapors under the simulated solar irradiation, CO, CH_4, H_2 and O_2 were produced by CO_2 reduction and H_2O oxidation. In general, several intermediates in the photocatalytic process of CO_2 reduction with H_2O are radical species, whose recombination at different stages partially accounts for the number of possible pathways and final products. The exact order and mechanistic details of each subsequent step have not been fully elucidated, but three full pathways detailing the conversion of CO_2 to CH_4 have been proposed in the literature. In the following discussion, they are referred to as 1) the formaldehyde pathway, 2) the carbene pathway, and 3) the glyoxal pathway on account of their unique intermediate.[9] For co-catalysts with coupling semiconductors with metal NPs, they have been shown to be beneficial for the performance of photocatalysts because of, among other factors, improved charge separation, facilitated CO_2 activation, and the provision of catalytic active sites for the reduction process. In a typical realization of this concept, the nanostructured semiconductor is surface-decorated with metal or metal oxide NPs. This architecture is utilized in almost all of the most efficient photocatalytic systems. It is a convenient setup which allows the catalytic process to be isolated from the light-harvesting and charge-separation functions of the photocatalyst.

Moreover, it is well-known that the design of photocatalysts for CO_2 reduction to CO and CH_4 must be meet the energy band theory, which is based on the relative positions of conduction band (CB), valence band (VB) and oxidation potentials. In general, photogenerated electrons can be consumed effectively, if the reduction potential of the reaction is lower than the CB-potential of the semiconductor. The possible reactions that can occur during photocatalytic CO_2 with H_2O to produce CO and CH_4 in terms of thermodynamic reduction potentials versus normal hydrogen electrode (NHE), can be described by reactions in Eqs. (1)-(4).

$$CO_2 + 2H^+ + 2e^- \rightarrow CO + H_2O \qquad E^\theta = -0.53V \qquad (1)$$

$$CO_2 + 8H^+ + 8e^- \rightarrow CH_4 + 2H_2O \qquad E^\theta = -0.24V \qquad (2)$$

$2H^+ + 2e^- \rightarrow H_2$ E^θ=-0.41V (3)

$2H_2O + 4h^+ \rightarrow 4H^+ + O_2$ E^θ=+0.82V (4)

The CB-potentials (E_{CB}) of TiO_2 and CdS are -0.56 and -1.0 V (vs. NHE at pH 7), respectively,[39] while the reduction potential of $E^\theta(CO_2/CO)$ is -0.53 V.[40] Since the CB flat band potential is more negative than the CO_2/CO reduction potential, the reduction reaction is theoretically feasible. For CO_2 reduction to CH_4, the lower reduction potential difference ($E^\theta(CO_2/CH_4)$=-0.24 V) also drove the reaction. Although the reduction potential of Eq. (2) is less negative than that of Eq. (1), eight electrons are required to produce CH_4 compared with only two electrons for CO production. Thus, it is significant to observe that the formation rates of CO and CH_4 in the gaseous products change with the nanostructure and composition of as-prepared catalysts.

Based on the results of the formation rates of H_2, CO and CH_4 (Table 3) and the nanostructure of 3DOM Pt@CdS/TiO_2 catalysts (Fig. 3), the enhanced photocatalytic activity for CO_2 reduction can be ascribed to their unique structure with a variety of favorable properties. On the one hand, 3DOM structure plays an important role for improving photocatalytic activity. 3DOM TiO_2 shows higher activity for CO_2 reduction than the commercial P25. 3DOM structure enhancement on the photocatalytic activity for CO_2 reduction could be easily understood due to improving the light-harvesting efficiency.[11b] On the other hand, the introduction of Pt@CdS core-shell NPs in CdS-Pt-TiO_2 nanojunction can effectively extend the spectral response from UV to visible area owing to the CdS-photosensitization and improve separation of photogenerated charge carriers.[23] According to the result of UV-Vis DRS, 3DOM Pt@CdS/TiO_2 catalysts show the super absorption efficiency for the simulated solar irradiation due to the synergistic effect of Pt@CdS core-shell NPs and 3DOM TiO_2 support. 3DOM Pt@CdS/TiO_2 catalysts consist of isolated photochemical system 1 (Pt/TiO_2), photochemical system 2 (CdS/Pt) and the electron-transfer system (Pt). After the absorption of photons, both TiO_2 and CdS are excited to produce electrion-hole pairs. For the isolated Pt/TiO_2 photochemical system, the generated electrons located at the CB of TiO_2 flow into Pt, i.e., electron transfer from TiO_2 to Pt. It is attributed to the different Fermi levels between Pt and the conduction band edge of TiO_2 and the formation of Schottky barrier at the interface of Pt and TiO_2. The VB-holes of TiO_2 with a strong oxidation power oxidize H_2O to O_2. Combined the results of XPS and catalytic performance, the electron conduction ability of Pt NPs improves with increasing amounts of $Pt^{\&+}$ species which have stronger ability to capture the electron from the CB of TiO_2 than metallic Pt species. For the isolated CdS/Pt photochemical system, the VB-holes of CdS could recombine with electrons derived from the Pt sensor because of the formation of the inner electric field with abundant electron over Pt nanoparticles, i.e., the electron transfer from Pt to CdS. And the CB-electrons of CdS would be used for CO_2 reduction rather than transferred to Pt because of the increase in their surface population in the Pt@CdS core-shell structure. Thus, the vectorial electron transfer of $TiO_2 \rightarrow Pt \rightarrow CdS$ should occur as a result of excitation of both TiO_2 and CdS under the conditions for CO_2 reduction. In other words, 3DOM Pt@CdS/TiO_2 catalyst is an all-solid-state Z-scheme system with CdS-Pt-TiO_2 nanojunction. In addition, the weight ratios of CdS/TiO_2 can adjust the amounts of photogenerated carriers in TiO_2 and CdS. 3DOM Pt@CdS/TiO_2-1 catalyst shows high catalytic activity and stability for the photocatalytic reduction of CO_2 with H_2O. It suggests that the amounts of the photogenerated electrons in TiO_2 and the photogenerated holes in CdS may achieve an optimization balance for neutralizing.

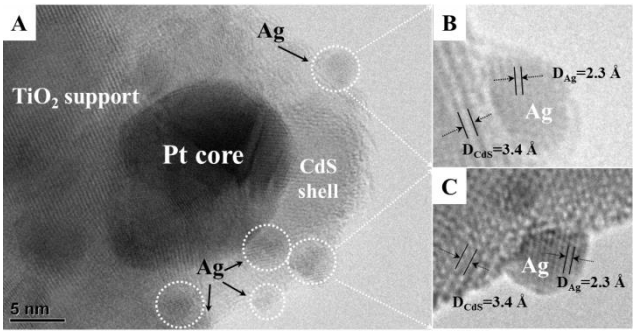

Fig. 9 HRTEM images of Ag/Pt@CdS/TiO_2 catalyst prepared by Ag photodeposition on the surface of 3DOM Pt@CdS/TiO_2-1 catalyst with UV- Vis light (320-780 nm) irradiation for 30 min. B and C images are the magnified images of Ag NP in A image.

In order to specify the reduction sites of Pt@CdS/TiO_2, Ag photodeposition experiment was carried out by irradiation with same light source of CO_2 reduction test for 30 min, and the result is shown in Fig. 9. The spherical Ag nanoparticles precipitated on the surface of Pt@CdS core-shell nanoparticles can be clearly observed in Fig. 9A. As shown in Fig. 9B-9C, the lattice fringes were clearly observed that the values of 2.3 and 3.4 Å are assigned to the (111) crystal faces of Ag nanoparticle with a cubic structure and CdS with a cubic hawleyite structure, respectively. It indicates that Ag particles supported on the surface of CdS shell. If the electron transfer from CdS to TiO_2 rapidly takes place through their contact with Pt, Ag NPs should be photodeposited on TiO_2. However, HRTEM images demonstrated that Ag nanoparitcles are deposited almost selectively on the surface of CdS shell layer and formation of the Ag photodeposited on Pt@CdS/TiO_2 (Ag/Pt@CdS/TiO_2). It indicates that CdS acts as the reduction sites of Pt@CdS/TiO_2 catalysts, and the back electron transfer from CdS to TiO_2 is a minor path, which strongly supports the vectorial electron transfer in the all-solid-state CdS-Pt-TiO_2 Z-scheme system. The Z-scheme system simultaneously generates VB-holes (TiO_2) with a strong oxidation power and CB-electrons (CdS) with a strong reduction power, which explains the high formation rates of CH_4 for CO_2 reduction.

On the basis of the above discussion, the mechanism for the photocatalytic reduction of CO_2 with H_2O over 3DOM Pt@CdS/TiO_2 catalysts was proposed and it is shown in Scheme 1. Firstly, 3DOM structure can improve the light-

harvesting efficiency, which is an important factor to enhance photocatalytic performance for CO_2 reduction. Secondly, the vectorial electron transfer of TiO_2→Pt→CdS over the all-solid-state Z-scheme system benefits the separation of photogenerated electrons and holes, which can increase the formation rates and selectivity of CH_4 for CO_2 reduction. Under the simulated solar irradiation, the electron-hole pairs are generated on the surface of both TiO_2 support and CdS shell. The generated electrons in the CB of TiO_2 flow into Pt NPs, and the electron further transfers to CdS shell and quenches with the VB-holes of CdS, which achieves the high separation efficiency of photogenerated electron-hole pairs in CdS-Pt-TiO_2 nanojunction system. Finally, the VB-holes of TiO_2 support can oxidize H_2O gathered on the surface of the catalyst and produce O_2 and H^+ protons. O_2 will desorption from the surface of catalysts to the gas, and H^+ protons may still stay in the absorbed H_2O film on the surface of catalysts, and they will migrate and gather to the surface of CdS due to the electrostatic gravity. Finally, the abundant CB-electrons of CdS shell with abundant H^+ protons would be used for CO_2 reduction and give priority to generating CH_4. Therefore, 3DOM Pt@CdS/TiO_2 catalysts, which take both advantages of the high light-harvesting efficiency by 3DOM supports and the high separation of photogenerated electrons and holes by the all-solid-state Z-scheme system with CdS-Pt-TiO_2 nanojunction, showed super photocatalytic performance for CO_2 reduction into CH_4 under the simulated solar irradiation.

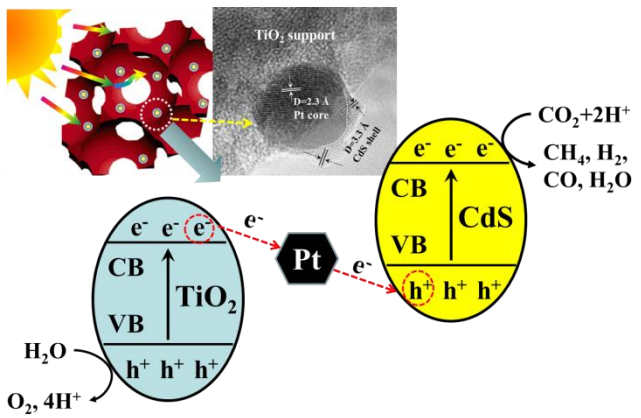

Scheme 1 The mechanism for the photoreduction of CO_2 with H_2O over 3DOM Pt@CdS/TiO_2 catalysts

4. Conclusions

We demonstrated a strategy for preparing the photocatalyst that consists of the core-shell-structured Pt@CdS NPs uniformly dispersed on 3DOM TiO_2 support via the GBMR/P method. The macropore structures of 3DOM Pt@CdS/TiO_2 catalysts are highly ordered and interconnected each other by small pore windows. 3DOM structure can improve the light-harvesting efficiency. The core-shell structural Pt@CdS NPs are highly dispersed on the inner walls of uniform macropores. The nanolayer thickness of the CdS shell over Pt NPs can be controlled at the nanoscale by the Cd/Pt molar ratio. The all-solid-state Z-scheme system with CdS(shell)-Pt(core)-TiO_2(support) nanojunction is favourable for the separation of photogenerated electrons and holes due to the vectorial electron transfer of TiO_2→Pt→CdS. 3DOM Pt@CdS/TiO_2 catalysts, which take both advantages of the high light-harvesting efficiency and the high separation of photogenerated electrons and holes, exhibited super photocatalytic performance for CO_2 reduction with H_2O to CH_4 under the simulated solar irradiation. Our design and versatile synthetic approach can potentially be extended to other nanoparticle cores with different compositions, sizes and shapes and to other shell compositions on the surface of 3DOM support. The fabrication of all-solid-state Z-scheme system on 3DOM oxides surface is expected to throw new light on the design of highly efficient photocatalyst for CO_2 reduction to hydrocarbon.

Acknowledgements

We acknowledge the financial support from the National Natural Science Foundation of China (No. 21177160 and 21303263), Beijing Nova Program (No. Z141109001814072), Specialized Research Fund for the Doctoral Program of Higher Education of China (No. 20130007120011) and Science Foundation of China University of Petroleum, Beijing (QZDX-2011-02, No. 2462013YJRC13 and 2462013BJRC003)

Notes and references

[a] State Key Laboratory of Heavy Oil Processing, Beijing Key Laboratory of Oil and Gas Pollution Control, China University of Petroleum,18#, Fuxue Road, Chang Ping, Beijing 102249, China, Fax: (+86) 10-89731586(O), E-mail: zhenzhao@cup.edu.cn; liujian@cup.edu.cn

† Footnotes should appear here. These might include comments relevant to but not central to the matter under discussion, limited experimental and spectral data, and crystallographic data.
Electronic Supplementary Information (ESI) available: Detailed description of experimental procedure; SEM, TEM images and size distribution of Pt nanoparticles; XRD and XPS characterizations. See DOI: 10.1039/b000000x/

a) S. C. Roy, O. K. Varghese, M. Paulose and C. A. Grimes, *ACS Nano*., 2010, **4**, 1259; b) F. Zuo, L. Wang, T, Wu, Z. Zhang, D. Borchardt and P. Feng, *J. Am. Chem. Soc*., 2010, **132**, 11856.

2 E. V. Kondratenko, G. Mul, J. Baltrusaitis, G. O. Larraz ́abal and J. Perez-Ramirez, *Energy Environ. Sci.*, 2013, **6**, 3112.

3 J. Lin, Z. Pan and X. Wang, *ACS Sustainable Chem. Eng.*, 2014, **2**, 353.

4 S. Zhou, Y. Liu, J. Li, Y. Wang, G. Jiang, Z. Zhao, D. Wang, A. Duan, J. Liu and Y. Wei, *Appl. Catal. B*., 2014, **158-159**, 20.

5 T. Inoue, A. Fujishima, S. Konishi and K. Honda, *Nature*, 1979, **277**, 637-640.

6 a) V. P. Indrakanti, J. D. Kubickib, H. H. Schobert, *Energy Environ. Sci.*, 2009, **2**, 745; b) K. Mori, H. Yamashita and M. Anpo, *RSC Adv.*, 2012, **2**, 3165; c) H. Zhou, J. Guo, P. Li, T. Fan, D. Zhang and J. Ye, *Sci. Rep*., 2013, **3**, 1667; d) J. Yu, J. Jin, B. Cheng and M. Jaroniec, *J. Mater. Chem. A*, 2014, **2**, 3407.

7 a) S. Xie, Y. Wang, Q. Zhang, W. Fan, W. Deng and Y. Wang, *Chem. Comm*., 2013, **49**, 2451; b) J. Zhao, X. Wang, Z. Xu and J. S. C. Loo, *J. Mater. Chem. A*, 2014, **2**, 15228; c) S. Yan, S. X. Ouyang, J. Gao, M. Yang, J. Feng, X. Fan, L. Wan, Z. Li, J. Ye, Y. Zhou and Z. Zou, *Angew. Chem*., 2010, **122**, 6544; d) K. Iizuka, T. Wato, Y. Miseki, K. Saito and A. Kudo, *J. Am. Chem. Soc*., 2011, **133**, 20863.

8 a) Y. Ma, X. Wang, Y. Jia, X. Chen, H. Han and C. Li, *Chem. Rev*., 2014, **114**, 9987; b) H. Xu, S. Ouyang, L. Liu, P. Reunchan, N. Umezawa and J. Ye, *J. Mater. Chem. A*, 2014, **2**, 12642; c) M. F. Lichterman, A. I. Carim, M. T. McDowell, S. Hu, H. B. Gray, B. S. Brunschwig and N. S. Lewis, *Energy Environ. Sci.*, 2014, **7**, 3334.

9 S. N. Habisreutinger, L. Schmidt-Mende and J. K. Stolarczyk, *Angew. Chem. Int. Ed*., 2013, **52**, 7372.

10 M. Pelaez, P. Falaras, A. G. Kontos, A. A. delaCruz, K. O'shea, P. S. M. Dunlop, J. A. Byrne and D. D. Dionysiou, *Appl. Catal. B*., 2012, **121-122**, 30.

11 a) J. I. L. Chen, G. Freymann, S. Y. Choi, V. Kitaev and G. A. Ozin. *Adv. Mater*., 2006, **18**, 1915; b) X. Cui, Y. Wang, G. Jiang, Z. Zhao, C. Xu, Y. Wei, A. Duan, J. Liu and J. Gao, *RSC Adv.*, 2014, **4**, 15689.

12 a) T. Kamegawa, N. Suzuki and H. Yamashita, *Energy Environ. Sci.*, 2011, **4**, 1411; b) N. Nishimura, N. Abrams, B. A. Lewis, L. I. Halaoui, T. E. Mal-louk, K. D. Benkstein, J. Lagemaat and A. J. Frank, *J. Am. Chem. Soc*., 2003, **125**, 6306; c) M. Wu, J. Jin, J. Liu, Z. Deng, Y. Li, O. Deparis and B. L. Su, *J. Mater. Chem. A*, 2013, **1**, 15491.

13 J. Liu, G. Liu, M. Z. Li, W. Z. Shen, Z. Liu, J. Wang, J. Zhao, L. Jiang and Y. Song, *Energy Environ. Sci*., 2010, **3**, 1503.

14 K. Koci, K. Mateju, L. Obalova, S. Krejcikova, Z. Lacny, D. Placha and L. Capek, *Appl. Catal. B*, 2010, **96**, 239.

15 S. Linic, P. Christopher and D. B. Ingram, *Nat. Mater*., 2011, **10**, 911.

16 a) X. Chen, X. Wang, Y. Hou, J. Huang, L. Wu and X. Fu, *J. Catal*., 2008, **255**, 59; b) M. Liu, X. Qiu, K. Hashimoto and M. Miyauchi, *J. Mater. Chem. A*, 2014, **2**, 13571.

17 a) H. G. Yang, C. H. Sun, S. Z. Qiao, J. Zou, G. Liu, S. C. Smith, H. M. Cheng and G. Q. Lu, *Nature*, 2008, **453**, 638; b) R. Li, F. Zhang, D. Wang, J. Yang, M. Li, J. Zhu, X. Zhou, H. Han and C. Li, *Nat. Commun*., 2013, **4**, 1432; c) H. Zhao, L. Liu, J. M. Andino and Y. Li, *J. Mater. Chem. A*, 2013, **1**, 8209.

18 a) J. Yang, D. Wang, H. Han, and C. Li, *Acc. Chem. Res*., 2013, **46**, 1900; b) S. Watanabe, X. Ma, C. Song, *J. Phys. Chem. C*, 2009, **115**, 14249.

19 Y. Xie, G. Ali, S. H. Yoo and S. O. Cho, *ACS Appl Mater. Interfaces*., 2010, **2**, 2910.

20 J. Tian, Y. Sang, Z. Zhao, W. Zhou, D. Wang, X. Kang, H. Liu, J. Wang, S. Chen, H. Cai and H. Huang, *Small*, 2013, **9**, 3864.

21 X. Chen, X. Wang and X. Fu, *Energy Environ. Sci.*, 2009, **2**, 872.

22 Q. Zhai, S. Xie, W. Fan, Q. Zhang, Y. Wang, W. Deng and Y. Wang, *Angew. Chem. Int. Ed*., 2013, **52**, 5776.

23 H. Tada, T. Mitsui, T. Kiyonaga, T. Akita and K. Tanaka, *Nat. Mater.*, 2006, **5**, 782.

24 a) S. Liu, M. Q. Yang and Y. J. Xu, *J. Mater. Chem. A*, 2014, **2**, 430; b) M. Zhang and X. Wang, *Energy Environ. Sci*., 2014, **7**, 1902; c) L. Wang, J. Ge, A. Wang, M. Deng, X. Wang, S. Bai, R. Li, J. Jiang, Q. Zhang, Y. Luo, and Y. Xiong, *Angew. Chem. Int. Ed.*, 2014, **53**, 5107.

25 K. Sayama, K. Mukasa, R. Abe, Y. Abe and H. Arakawa, *Chem. Commun*., 2001, 2416.

26 B. S. Veldkamp, W. S. Han, S. M. Dyar, S. W. Eaton, M. A. Ratner and M. R. Wasielewski, *Energy Environ. Sci.*, 2013,**6**, 1917.

27 a) Y. Wei, J. Liu, Z. Zhao, A. Duan, G. Jiang, C. Xu, J. Gao, H. He, X. Wang, *Energy Environ. Sci.*, 2011, **4**, 2959; b) Y. Wei, J. Liu, Z. Zhao, Y. Chen, C. Xu, A. Duan, G. Jiang, H. He, *Angew. Chem. Int. Ed.*, 2011, **50**, 2326; c) Y. Wei, J. Liu, Z. Zhao, A. Duan, G. Jiang, *J. Catal.*, 2012, **287**, 13.

28 Y. Wei, Z. Zhao, J. Liu, S. Liu, C. Xu, A. Duan, G. Jiang, *J. Catal.*, 2014, **317**, 62.

29 Y. Wei, Z. Zhao, X. Yu, B. Jin, J. Liu, C. Xu, A. Duan, G. Jiang and S. Ma, *Catal. Sci. Technol.*, 2013, **3**, 2958.

30 M. Yoon, M. Seo, C. Jeong, J. H. Kang and K. S. Jeon, *Chem. Mater.*, 2005, **17**, 6069.

31 J. Fang, X. Bi, D. Si, Z. Jiang and W. Huang, *Appl. Surf. Sci.*, 2007, **253**, 8952.

32 H. Cao, G. Wang, S. Zhang, X. Zhang and D. Rabinovich, *Inorg. Chem.*, 2006, **45**, 5103.

33 P. Kundu, P.A. Deshpande, G. Madras and N. Ravishankar, *J. Mater. Chem.*, 2011, **21**, 4209.

34 C. Harding, V. Habibpour, S. Kunz, A. N. Farnbacher, U. Heiz, B. Yoon and U. Landman, *J. Am. Chem. Soc.*, 2009, **131**, 538.

35 F. X. Xiao, J. Miao and B. Liu, *J. Am. Chem. Soc.*, 2014, **136**, 1559.

36 J. Tian, Y. Sang, Z. Zhao, W. Zhou, D. Wang, X. Kang, H. Liu, J. Wang, S. Chen, H. Cai and H. Huang, *Small*, 2013, **9**, 3864.

37 Y. Lei, L. D. Zhang, G. W. Meng, G. H. Li, X. Y. Zhang, C. H. Liang, W. Chen and S. X. Wang, *Appl. Phys. Lett.*, 2001, **78**, 1125.

38 L. Spanhel, H. Weller and A. Henglein, *J. Am. Chem. Soc.*, 1987, **109,** 6632.

39 S. Sakthivel, M. C. Hidalgo, D. W. Bahnemann, S. U. Geissen, V. Murugesan and A. Vogelpohl, *Appl. Catal. B*, 2006, **63**, 31.

40 E. E. Benson, C. P. Kubiak, A. J. Sathrum and J. M. Smieja, *Chem. Soc. Rev*., 2009, **38**, 89.

Graphical Abstract

3DOM Pt@CdS/TiO_2 catalysts exhibit super photocatalytic performance for CO_2 reduction with H_2O to CH_4 under the simulated solar irradiation.